A Novel Approach for Representing Ice Microphysics in Models: Description and Tests Using a Kinematic Framework

HUGH MORRISON AND WOJCIECH W. GRABOWSKI

National Center for Atmospheric Research, Boulder, Colorado*

(Manuscript received 4 April 2007, in final form 21 August 2007)

ABSTRACT

This paper documents the development of a novel approach for representing ice microphysics in numerical models. In this approach, the ice particle mass–dimension and projected-area–dimension relationships vary as a function of particle size and rimed mass fraction. All ice microphysical processes and parameters are calculated in a self-consistent manner in terms of these mass–dimension and area–dimension relationships. The rimed mass fraction is predicted locally by separately predicting the ice mixing ratios acquired through water vapor deposition and through riming. The third predicted variable is the number concentration of ice particles. This approach allows representing in a natural way the gradual transition from small to large ice particles due to growth by water vapor deposition and aggregation and from unrimed crystals to graupel due to riming. In traditional approaches, these processes are treated by separating ice particles into predefined categories (such as cloud ice, snow, and graupel) using fairly arbitrary thresholds and conversion rates. With some modifications, the new approach can be employed in either bin or bulk microphysical models.

In this paper, the new approach is implemented in a bulk two-moment microphysical scheme representing both warm-rain and ice processes and it is applied to an idealized 2D kinematic framework mimicking a shallow mixed-phase cumulus. The size distributions of cloud droplets, drizzle/rain drops, and ice particles are represented using gamma distributions. The new scheme is compared to a version of the scheme that uses the traditional approach for ice microphysics; that is, unrimed ice/snow and graupel are separate species, with threshold-based conversion rates between the former and the latter. The new and traditional schemes produce similar results, although the traditional scheme, unlike the new scheme, produces a distinct double maximum in the surface precipitation rate, corresponding to precipitation shafts consisting of either ice/snow or graupel. The relative magnitude of these peaks, as well as the ice water path and optical depth of the simulated cloud, is highly sensitive to the threshold for converting unrimed ice to graupel. In contrast, the new scheme does not require any conversion threshold and predicts formation of ice particles with wide range of rimed fractions.

1. Introduction

The representation of ice microphysics in models has a significant impact on quantitative precipitation forecasts (e.g., Rutledge and Hobbs 1984; Gilmore et al. 2004; Thompson et al. 2004), prediction of supercooled liquid water (e.g., Reisner et al. 1998; Thompson et al. 2004; Morrison and Pinto 2006), simulations of radiative transfer in clouds (e.g., Gu and Liou 2000; Wu 2002), and cloud dynamical interactions (e.g., Leary and Houze 1979; Lord et al. 1984; Zhang and Gao 1989; McFarquhar et al. 2006). Microphysics schemes are classified broadly into two types: (i) bin schemes and (ii) bulk schemes. Bin schemes predict the particle size distribution (PSD) by discretizing it explicitly into multiple size (or mass) bins. Bulk schemes predict one or more bulk quantities and assume some underlying form for the PSD. Bin schemes are less restrictive because they allow the size distribution to evolve, but they are computationally demanding. Furthermore, many of the uncertainties associated with bulk microphysics schemes apply to bin schemes as well. The one-moment bulk approach was first applied by Kessler (1969) to warm (ice free) clouds based on the natural separation

* The National Center for Atmospheric Research is sponsored by the National Science Foundation.

Corresponding author address: Hugh Morrison, NCAR, P.O. Box 3000, Boulder, CO 80307-3000.
E-mail: morrison@ucar.edu

DOI: 10.1175/2007JAS2491.1

between cloud droplets and drizzle/rain. This separation corresponds to the rapid growth of drizzle drops (once they are initiated) due to accretion of cloud droplets, producing a distinct minimum in the drop size spectrum between about 30 and 50 μm (e.g., Berry and Reinhardt 1973). Thus, mixing ratio was separately predicted for each category (cloud droplets and drizzle/rain drops), with parameterized conversion rates (autoconversion and accretion) transferring the cloud water to drizzle/rain. More detailed two-moment schemes were subsequently developed that predict both mixing ratio and number concentration of cloud droplets and drizzle/rain (e.g., Khairoutdinov and Kogan 2000; Seifert and Beheng 2001; Saleeby and Cotton 2004; Morrison et al. 2005). These schemes are potentially more robust since they allow the mean particle size to evolve as a free parameter. They also provide a more realistic treatment of cloud–aerosol interactions since cloud condensation nuclei (CCN) directly impact the droplet number concentration through nucleation processes.

The bulk approach was extended to the ice phase using a similar separation between cloud ice and large precipitating ice (e.g., Lin et al. 1983; Rutledge and Hobbs 1984; Dudhia 1989; Ferrier 1994; Meyers et al. 1997; Reisner et al. 1998; Milbrandt and Yau 2005). This separation was required since the empirical particle fall speed–size relationships used in these schemes apply to only a limited size range (thus requiring separation of small and large ice particles). This approach also represents a legacy of the Kessler-type warm scheme. However, the distinction between small and large particle modes is less clear for ice than liquid because large precipitating ice particles can be produced by both accretional and vapor depositional growth; rain is produced by accretional growth only. Precipitation ice is often further subdivided into different predefined categories (e.g., snow, aggregates, graupel, hail). The parameters needed for calculating microphysical process rates are specified a priori for each predefined ice category. A similar separation of unrimed crystals, graupel, and/or hail is employed by many bin microphysics models (e.g., Geresdi 1998; Ovtchinnikov and Kogan 2000; Rasmussen et al. 2002).

A key point is that in nature the boundaries between different ice categories (cloud ice, snow, graupel, hail) are difficult to define and transitions between various categories happen gradually. For instance, as ice crystals grow by diffusion of water vapor and aggregation, their mass and terminal velocities gradually increase, and they gradually move from the "cloud ice" into the "snow" category. The same is true for the growth by riming, where ice particles gradually increase their mass and rimed mass fraction and move from the "snow" to the "graupel" category. In traditional schemes, there are no transitional regimes between various ice categories and conversion of ice from one category to another occurs in a single discrete step. For example, some schemes produce graupel immediately after a minimum riming rate or mixing ratio is reached. More detailed models prognose the particle density to more accurately determine the threshold for conversion to graupel (e.g., Ferrier 1994). However, none of these schemes treat the transitional regimes that represent the growth of a small ice particle into a large ice crystal or an aggregate (i.e., the snowflake) or growth of a rimed crystal into a graupel particle. This has the potential to produce undesirable thresholding behavior; that is, model solutions may diverge depending whether a particular threshold (e.g., the cloud ice mixing ratio or the riming rate) is reached or not. Thus, significant sensitivity of the simulated clouds and precipitation to these thresholds has been noted (e.g., Rutledge and Hobbs 1984; Thompson et al. 2004); these thresholds must therefore be tuned to produce desirable results. For the conversion from cloud ice to snow, a more appropriate approach is, for instance, to smoothly predict the evolution of crystal habit and terminal velocity during the transition from small to large crystals. A more realistic description of the growth of rimed crystals into graupel follows the conceptual model of Heymsfield (1982). In this framework, single crystals and aggregates are converted to graupel through a "filling in" process in which droplets are collected in the interstices between crystal branches. This process results in an increase of the particle mass, but not the particle dimension D. Eventually, filling in of the unoccupied volume results in an ice spheroid (graupel) of dimension D. At this point, further growth of the particle increases both mass and dimension. The time required to fill in the crystal volume by riming to produce graupel can be significant (several minutes) under realistic environmental conditions, especially for large crystals (see Heymsfield 1982, Fig. 7).

Specifying the parameters needed for the microphysical calculations requires explicit or implicit assumption of the crystal habit. Some schemes diagnose the habit based on local conditions (e.g., temperature, relative humidity); see Meyers et al. (1997). The most detailed schemes allow the crystal habit to evolve according to the degree of riming, rate of depositional growth along the major and minor axes, and aggregation (Chen and Lamb 1994; Hashino and Tripoli 2007). These schemes provide a potentially more robust solution because they retain the particle history and therefore calculate relevant parameters directly from the model variables rather than assuming fixed values for

predefined ice categories. However, there remain uncertainties since the crystal growth rates are not well characterized across the range environmental conditions, and the habit may itself depend on the nucleating mechanism (Bailey and Hallett 2002). Note that there are many other uncertainties in parameterizing ice microphysics including primary ice nucleation, fragmentation and secondary crystal initiation, and sticking efficiency for ice–ice collisions.

In this paper, we propose a novel approach for parameterizing ice microphysics that shifts away from the traditional approach of predefined ice categories. Our approach allows the crystal habit and associated microphysical parameters to evolve during the simulation based on the particle history, similar to Hashino and Tripoli (2007). However, for simplicity we do not retain the history of differential axis growth due to vapor deposition or aggregation, but do allow the habit to evolve according to the rimed mass fraction of the crystal. The history of the rimed mass fraction is retained by predicting two ice mixing ratio variables: (i) the mixing ratio due to vapor deposition and (ii) the mixing ratio due to riming. It follows that the rimed mass fraction is derived locally from the ratio of the riming and total (riming plus deposition) mixing ratios. This approach allows the mass–dimension (m–D) and projected area–dimension (A–D) relationships to evolve according to the predicted rimed mass fraction and particle dimension. All relevant microphysical parameters in the scheme are based on these m–D and A–D relationships for self-consistency. This approach removes the need for arbitrary thresholds for conversions of small ice to snow during vapor deposition and/or aggregation, and conversion of crystals to graupel during riming. The goal is to provide a physically based treatment of the ice microphysics that accounts for the transitional regimes and avoids thresholding behavior while retaining a relatively simple and flexible framework.

This paper documents the extension of an existing two-moment warm bulk microphysics scheme (Morrison and Grabowski 2007) to the ice phase using this new approach. The conversion of rimed crystals into graupel is based on Heymsfield's conceptual model, described above, that relates the particle mass and dimension to the riming growth and filling in of crystal interstices. Since the scheme predicts mean particle size and includes a smooth transition in the m–D and A–D relationships between small and large crystals, the gradual conversion of cloud ice to snow is represented in a natural way. Thus, the nonphysical autoconversion process used in most bulk models to transfer mass and number between the cloud ice and snow categories is not needed. The transition between small and large ice during growth by vapor deposition and aggregation is calculated using m–D and A–D relationships that vary smoothly across the PSD for different particle sizes. Relevant parameters (e.g., terminal particle fall speeds) are calculated in a self-consistent manner over the entire PSD from these m–D and A–D relationships. Note that, although we apply the new approach in a bulk model, it could also be readily applied to bin models. In bin models the rimed mass fraction would be retained locally for each size or mass bin and then used to derive the m–D and A–D relationships in each bin.

The new scheme is tested using a kinematic framework. The kinematic framework includes a specified flow field that allows for testing of the microphysics scheme without complications due to cloud dynamical feedbacks, but it includes the critical processes of gravitational and advective transport. The specified flow field corresponds to an idealized shallow cumulus described in Szumowski et al. (1998) and Morrison and Grabowski (2007). The new scheme is contrasted with a corresponding version of the scheme that uses the traditional approach with predefined ice categories for ice/snow and graupel. The paper is organized as follows. Section 2 describes the new scheme. Section 3 describes the kinematic modeling framework and the specific case applied here. Section 4 describes results including sensitivity tests, and section 5 gives summary and conclusions.

2. Description of the new microphysics scheme

The two-moment bulk warm rain scheme of Morrison and Grabowski (2007; hereafter MG07) has been extended to the ice phase using the novel approach outlined in the introduction. The warm microphysics component is detailed in MG07, while the new ice component is described in this section.

As mentioned in the introduction, all ice microphysical processes and parameters are calculated consistently in terms of the particle mass–dimension and projected area–dimension relationships. These relationships are obtained across the whole range of particle sizes using observationally based relations for different types of ice particles (available in the literature) and the rimed mass fraction predicted by the model. The history of rimed mass fraction is retained by predicting separately the mixing ratios of ice due to the vapor deposition q_{dep} and due to riming q_{rim}. The change in ice mixing ratio due to water vapor deposition and initiation of ice by deposition/condensation freezing and freezing of cloud droplets contributes to q_{dep}. The change in ice mixing ratio due to collisions between ice particles and cloud droplets/rain (in subfreezing condi-

tions) and ice initiation due to freezing of raindrop contributes to $q_{\rm rim}$. Sublimation and melting (including melting due to rain–ice collisions above freezing) are applied to both $q_{\rm dep}$ and $q_{\rm rim}$.

Since we also predict the ice number concentration N, there are a total of three prognostic variables for ice in the scheme. The time evolution of these three prognostic variables is given by

$$\frac{\partial N}{\partial t} + \frac{1}{\rho_a}\boldsymbol{\nabla}\cdot[\rho_a(\mathbf{u} - V_N\mathbf{k})N] = \mathcal{F}_N \equiv \left(\frac{\partial N}{\partial t}\right)_{\rm nuc} + \left(\frac{\partial N}{\partial t}\right)_{\rm sub} + \left(\frac{\partial N}{\partial t}\right)_{\rm frz} + \left(\frac{\partial N}{\partial t}\right)_{\rm mlt} + \left(\frac{\partial N}{\partial t}\right)_{\rm mult} + \left(\frac{\partial N}{\partial t}\right)_{\rm agg} + \left(\frac{\partial N}{\partial t}\right)_{\rm mltc} + \mathcal{D}(N), \quad (1)$$

$$\frac{\partial q_{\rm dep}}{\partial t} + \frac{1}{\rho_a}\boldsymbol{\nabla}\cdot[\rho_a(\mathbf{u} - V_q\mathbf{k})q_{\rm dep}] = \mathcal{F}_{q_{\rm dep}} \equiv \left(\frac{\partial q_{\rm dep}}{\partial t}\right)_{\rm nuc} + \left(\frac{\partial q_{\rm dep}}{\partial t}\right)_{\rm dep} + \left(\frac{\partial q_{\rm dep}}{\partial t}\right)_{\rm sub} + \left(\frac{\partial q_{\rm dep}}{\partial t}\right)_{\rm frz} + \left(\frac{\partial q_{\rm dep}}{\partial t}\right)_{\rm mlt} + \left(\frac{\partial q_{\rm dep}}{\partial t}\right)_{\rm mltc} + \mathcal{D}(q_{\rm dep}), \quad (2)$$

$$\frac{\partial q_{\rm rim}}{\partial t} + \frac{1}{\rho_a}\boldsymbol{\nabla}\cdot[\rho_a(\mathbf{u} - V_q\mathbf{k})q_{\rm rim}] = \mathcal{F}_{q_{\rm rim}} \equiv \left(\frac{\partial q_{\rm rim}}{\partial t}\right)_{\rm frz} + \left(\frac{\partial q_{\rm rim}}{\partial t}\right)_{\rm mlt} + \left(\frac{\partial q_{\rm rim}}{\partial t}\right)_{\rm sub} + \left(\frac{\partial q_{\rm rim}}{\partial t}\right)_{\rm accc} + \left(\frac{\partial q_{\rm rim}}{\partial t}\right)_{\rm accr} + \left(\frac{\partial q_{\rm rim}}{\partial t}\right)_{\rm mltc} + \mathcal{D}(q_{\rm rim}), \quad (3)$$

where $\mathbf{u}$ is the wind velocity vector; ρ_a is the air density profile; V_N and V_q are the number- and mass-weighted mean particle fall speeds, respectively; $\mathbf{k}$ is a unit vector in the vertical direction; and $\mathcal{D}$ is the subgrid-scale turbulent mixing operator (set to zero in the current study). The symbolic terms on the right-hand side of (1)–(3) represent the source/sink terms for N, $q_{\rm rim}$, and $q_{\rm dep}$. These include primary nucleation on aerosol through deposition or condensation–freezing (subscript nuc), vapor deposition (subscript dep), sublimation (subscript sub), freezing of cloud droplets and rain (subscript frz), melting (subscript mlt), ice multiplication (subscript mult; N only), aggregation of ice (subscript agg; N only), collection of cloud droplets (subscript accc; $q_{\rm rim}$ only), freezing of rain due to ice–rain collisions in subfreezing conditions (subscript accr; $q_{\rm rim}$ only), and melting of ice due to ice–rain collisions in above freezing conditions (subscript mltc). To ensure consistency between N and total ice mixing ratio in the code, the mean ice particle size is restricted to the range between 1 and 5000 μm; N is adjusted if these bounds are exceeded. Formulations for the various microphysical processes are described in the appendix. For the sink terms (sublimation and melting, including melting due to ice–rain collisions), the tendencies of $q_{\rm rim}$ and $q_{\rm dep}$ are given by formulations described in the appendix multiplied by the relative contributions of $q_{\rm rim}$ and $q_{\rm dep}$ to the total ice mixing ratio.

Similarly to the liquid species (cloud droplets and rain) described in MG07, the ice PSD follows a generalized gamma distribution:

$$N(D) = N_o D^{\mu} e^{-\lambda D}, \quad (4)$$

where D is the particle dimension (hereafter dimension refers to length of the major axis), N_0 is the "intercept" parameter, λ is the slope parameter, and $\mu = 1/\eta^2 - 1$ is the spectral shape parameter (η is the relative radius dispersion, the ratio between the standard deviation and the mean radius). These size distribution parameters are needed for calculation of the various microphysical process rates in (1)–(3).

For cloud droplets and rain, μ is specified following

MG07. For ice, μ is specified as a function of λ following Heymsfield (2003):

$$\mu = 0.076\lambda^{0.8} - 2, \tag{5}$$

where λ has units of cm^{-1}. This expression was obtained from gamma PSD fits to tropical and midlatitude particle ensembles in ice clouds (see Heymsfield 2003). Because the fitted PSDs are extrapolated for particles smaller than 50 μm, this expression is more uncertain for larger values of λ (implying smaller mean size). In the code, μ is limited to $0 \leq \mu \leq 6$, although Heymsfield (2003) shows negative values of μ for $\lambda < \sim 70$ cm^{-1}. Here we constrain μ to be positive so that $N(D)$ is finite at $D = 0$.

Parameters N_0 and λ can be found by relating the PSD to the predicted number concentration N and mixing ratio q (note that, for ice, $q = q_{\text{dep}} + q_{\text{rim}}$):

$$N = \int_0^\infty N(D)\, dD, \tag{6}$$

$$q = \int_0^\infty m(D)N(D)\, dD, \tag{7}$$

where $m(D)$ is the particle mass and $N(D)$ is given by (4). A solution for the size distribution parameters N_0 and λ in terms of μ, N, and q using (5)–(7) requires specification of the m–D relationship across the PSD. For cloud droplets and rain, this is given by $m = \pi/6\rho_w D^3$, where ρ_w is the bulk density of liquid water. Note that, although the A–D relationship is not used to derive the size distribution parameters using (5)–(7), it is needed, along with the size distribution parameters and m–D relationship, for calculation of several of the process rates in (1)–(3) (e.g., collection of cloud water and rain by ice particles). For cloud droplets and rain, the A–D relationship is simply given by $A = \pi D^2/4$.

For the ice phase, a complication arises because the m–D and A–D relationships vary as a function of crystal habit, degree of riming, and particle size. Thus, by predicting both q_{dep} and q_{rim} and retaining the history of bulk rimed mass fraction F_r [$F_r \equiv q_{\text{rim}}/(q_{\text{rim}} + q_{\text{dep}})$], we seek to provide a physical basis for the evolution of m–D and A–D relations across a wide range of conditions. The m–D and A–D relationships as a function of crystal habit, rimed mass fraction, and particle size are detailed below. First, we describe a relatively straightforward situation for unrimed crystals and subsequently turn our attention to the significantly more complicated case of rimed ice particles.

For unrimed crystals, we assume that small crystals may be approximated as solid ice spheres with an effective density equal to that of bulk ice $\rho_i \approx 0.9$ g cm^{-3} (Heymsfield et al. 2007a). It follows that the m–D and A–D relationships for small ice particles are

TABLE 1. Coefficients used in the baseline runs for the mass–dimension relationship, where $m = \alpha D^\beta$, and the projected area–dimension relationship, where $A = \sigma D^\gamma$, for the different ice particle types described in the text (cgs units). The bulk density of ice is $\rho_i \approx 0.9$ g c m^{-3}.

Particle type	m–D		A–D	
	α	β	σ	γ
Spherical ice	$\pi\rho_i/6$	3	$\pi/4$	2
Dense nonspherical/unrimed, nonspherical	0.00142	2.02	0.55	1.97
Graupel	0.049	2.8	0.625	2
Partially rimed	See text		See text	

$$m_s = \alpha_s D^{\beta_s} = \frac{\pi}{6}\rho_i D^3, \tag{8}$$

$$A_s = \sigma_s D^{\gamma_s} = \frac{\pi}{4} D^2, \tag{9}$$

where m_s and A_s are the mass and projected area of the ice particle. Larger unrimed crystals, whether grown by vapor deposition or aggregation, are generally nonspherical and have an effective density significantly less than ρ_i. The m–D and A–D relationships for these crystals are typically expressed by power laws:

$$m_i = \alpha_i D^{\beta_i}, \tag{10}$$

$$A_i = \sigma_i D^{\gamma_i}, \tag{11}$$

where m_i and A_i are the mass and projected area of the larger nonspherical, unrimed ice crystals. The m–D and A–D relationships for these larger crystals are dependent upon the crystal habit. Here the m–D and A–D parameters (Table 1) are for platelike crystals with sector branches (P1b) (Mitchell 1996). For conditions in the shallow cumulus simulated here (see section 3), that is, $-10°$ to $-15°$C and near water saturation, platelike crystals with sector branches are a reasonable assumption (e.g., see Pruppacher and Klett 1997, Figs. 2–36a).

Empirical m–D and A–D relationships for nonspherical crystals apply only to a limited size range (e.g., Mitchell 1996 and references therein). To create a smooth transition between small spherical ice and larger nonspherical crystals and aggregates, we extrapolate—following Heymsfield et al. (2007a)—the m–D relationship for larger nonspherical crystals down to a threshold dimension D_{th} such that $m_i = m_s$ for $D = D_{\text{th}}$. From (8) and (10) one obtains

$$D_{\text{th}} = \left(\frac{\pi\rho_i}{6\alpha_i}\right)^{1/(\beta_i - 3)}. \tag{12}$$

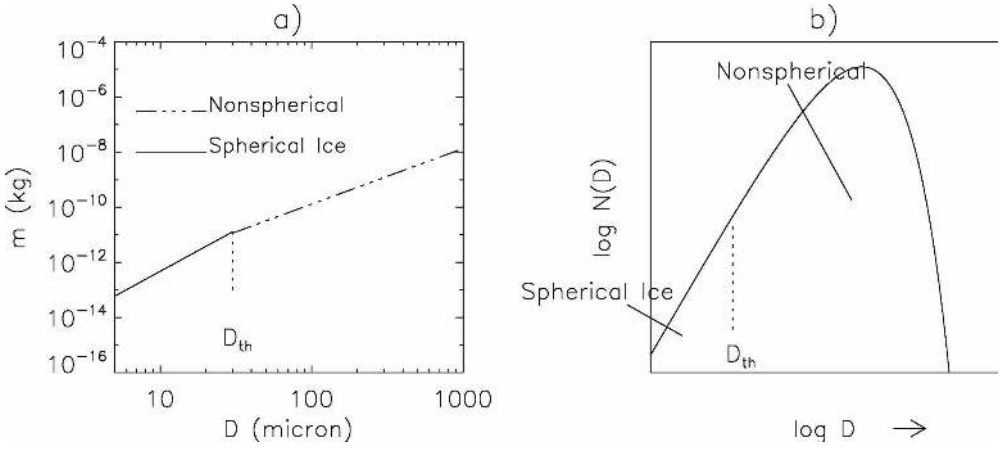

FIG. 1. (a) Mass–dimension relationships in unrimed conditions for solid spherical ice and unrimed nonspherical ice using parameters in Table 1 and critical particle dimension D_{th}. (b) Schematic diagram of the gamma particle size distribution $N(D)$ divided into two regions based on D_{th}.

For the selected set of m–D coefficients (see Table 1), $D_{th} \approx 30$ μm. It must be emphasized that D_{th} is not arbitrarily chosen but is instead completely determined by the m–D relationship for the larger nonspherical crystals.

It follows that, for the case with no riming, the m–D and A–D relationships valid across the whole range of ice particle sizes is found by dividing the PSD into two regions based on D_{th}: 1) particles with $D < D_{th}$ have m–D and A–D following solid ice spheres, and 2) particles with $D > D_{th}$ have m–D and A–D following unrimed nonspherical ice crystals. This is illustrated in Fig. 1. A key point is that this approach allows for a smooth transition in m–D between small ice and larger ice particles grown by vapor deposition and/or aggregation, as opposed to using separate cloud ice and snow categories as in most other bulk ice schemes. Note that, since this partitioning of the PSD is applied to A–D as well as m–D, there are small discontinuities in A–D between the regions. However, for the m–D and A–D relationships used here (see Table 1), the relative difference in projected area between the two regions at D_{th} is only 17.5%. A fairly simple interpolation could be added to remove this small discontinuity in A–D.

Under conditions allowing riming, the situation is significantly more complicated. In the absence of observations, we assume that the bulk rimed mass fraction predicted by the model applies to the entire spectrum of ice particles except for small ice crystals, which are not supposed to grow by riming (this aspect is discussed in the appendix). This assumption is justified by comparing the mass growth rate due to riming with the scaling of mass with D for crystals grown by vapor diffusion and aggregation. The mass growth rate due to riming, $dm_{rim}(D)/dt$, is proportional to the gravitational collection kernel; that is, $dm_{rim}(D)/dt \sim EVA$, where E is the collection efficiency, V is the ice particle fall speed, and A is the ice particle projected area (sticking efficiency is assumed to be unity). Numerical calculations suggest that the collection efficiency of cloud droplets by ice particles increases with ice particle dimension for platelike and broad-branch crystals smaller than about 500 μm, but is fairly constant for crystals larger than this size (see Wang and Ji 2000, Figs. 6 and 7 therein). Given that the fall speed of larger crystals is nearly constant with size (e.g., Mitchell 1994) and A is approximately proportional to D^2, this suggests that the collision kernel for larger crystals is approximately proportional to D^2. This is similar to the approximate scaling of mass with D observed for crystals grown by vapor diffusion and aggregation; that is, $m \sim D^2$ (e.g., Mitchell 1996). Hence, assuming that the scaling of rimed mass with D is similar to the scaling of the growth rate due to riming with D, the fraction of crystal mass grown by riming should be mostly independent of size, at least for larger crystals. This assumption breaks down for smaller crystals (<500 μm), whose collection efficiency and particle fall speed both increase with particle dimension. This assumption is also uncertain for large graupel particles (larger than a few millimeters) whose collection efficiency actually decreases with increasing particle size (Cober and List 1993). (Future work should test the assumption of constant F_r with D more rigorously using a bin modeling approach that explicitly predicts the change of rimed mass fraction with particle size using detailed expressions for collection efficiency as a function of particle dimension over the range of particle sizes. Note that the approach developed here

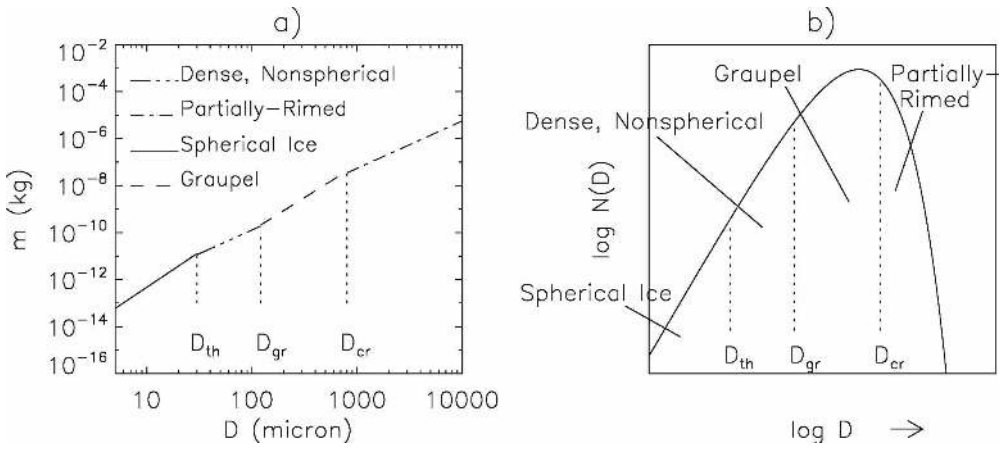

FIG. 2. (a) Mass–dimension relationships in rimed conditions for solid spherical ice, graupel, dense nonspherical ice, and partially rimed ice using parameters in Table 1, and critical dimensions D_{th}, D_{gr}, and D_{cr}. The m–D relationship shown in this example is calculated using a rimed mass fraction of 0.75. (b) Schematic diagram of the gamma particle size distribution $N(D)$ divided into four regions based on D_{th}, D_{gr}, and D_{cr}.

could be modified to include a rimed mass fraction that varies with D).

As explained below, our approach requires that the PSD is divided into four regions, referred to as (from the smallest to the largest) small ice spheres, dense nonspherical crystals, graupel, and partially rimed crystals; see Fig. 2. The four regions are bounded by three critical particle dimensions: D_{th}, D_{gr}, and D_{cr}. The dimension D_{th} was described previously for the case with no riming. The necessity of D_{cr} and D_{gr} is explained below. The key point is that these regions are partitioned in such a way as to produce smooth transitions in the m–D relationship, even though these relationships differ for the different ice particle types, as shown in Fig. 2a (e.g., different slopes seen in the m–D relationship for different particle types). We emphasize that D_{th}, D_{gr}, and D_{cr} are not arbitrarily chosen but, instead, are completely determined by the m–D relationships for dense nonspherical crystals and graupel and the rimed mass fraction as described below.

The m–D relationship for rimed ice crystals as a function of the rimed mass fraction F_r is derived from the basic conceptual model of Heymsfield (1982). Based on this model, rime accumulation in the crystal interstices increases the particle mass but not the particle dimension D, and such a picture is valid up to the point of a complete filling in of crystal interstices. From this point the particle becomes a graupel and further riming increases both particle size and mass. Prior to the complete filling in of the interstices, the rimed mass fraction of an individual crystal is assumed equal to the bulk rimed fraction F_r and the particle dimension D is determined by the crystal mass grown by diffusion of water vapor and aggregation m_i. If the total mass of rimed particle is m_r, then it follows that the mass fraction F_r is

$$F_r = \frac{m_r - m_i}{m_r}. \tag{13}$$

Assuming that the m–D relationship for rimed crystals follows a power law $m_r = \alpha_r D^{\beta_r}$, and the m–D relationship for m_i is given by (10), then (13) implies that

$$\alpha_r D^{\beta_r} = \frac{\alpha_i}{(1 - F_r)} D^{\beta_i}. \tag{14}$$

Since we assume constant F_r with D and (14) holds true for arbitrary D, then $\alpha_r = \alpha_i/(1 - F_r)$ and $\beta_r = \beta_i$. It follows that the m–D relationship for partially rimed crystals is

$$m_r = \left(\frac{1}{1 - F_r}\right)\alpha_i D^{\beta_i}. \tag{15}$$

Rogers (1974) found that the β parameter in the m–D relationship is the same for both rimed and unrimed snowflakes, consistent with our assumptions above, while the α is about 4 times larger for rimed compared to unrimed snow. Using a rimed mass fraction of 75% in (15) produces results consistent with these observations. A key point is that the m–D relationship given by (15) for partially rimed crystals follows logically from Heymsfield's conceptual model and the assumption of constant F_r with D. Since this conceptual model does not provide direct information on the evolution of A during riming growth, the A–D relationship for partially rimed crystals is found by linear interpolation be-

tween the projected area for the crystal grown by aggregation and vapor diffusion [given by Eq. (11)] and the projected area for graupel [given Eq. (17) below], based on F_r. Note that at values of F_r approaching unity, partially rimed crystals are filled in with rime and (15) is no longer valid (this is detailed below). Thus, we avoid the singularity resulting from the factor of $(1 - F_r)$ in the denominator of (15).

As the rimed mass fraction increases, complete filling in of the crystal interstices occurs. At this point the particle is considered graupel and further growth follows the m–D and A–D relationships for graupel, expressed by power laws as

$$m_g = \alpha D^{\beta_g}, \tag{16}$$

$$A_g = \sigma_g D^{\gamma_g}, \tag{17}$$

where m_g and A_g are the mass and projected area of the graupel particle. Rime density is not explicitly considered here; rather, it is implicit in the specified m–D relationship for graupel given by (16). Here the m–D parameters in (16) are for lump graupel following Heymsfield and Kajikawa (1987; see Table 1). Since the A–D for graupel is not given by Heymsfield and Kajikawa (1987), we use the formulation for hail following Matson and Huggins (1980; see Table 1).

Since the empirical m–D relationships for unrimed ice and graupel are such that $\beta_i < \beta_g$ (i.e., the rate of increase of mass with diameter is greater for graupel than it is for unrimed nonspherical crystals), small crystals will fill in with rime (i.e., attain a mass equal to that of a graupel particle of the same dimension) at smaller values of F_r than large crystals. Thus, if the rimed fraction F_r is assumed constant across the entire range of ice particle sizes, there has to exist a critical dimension $D_{\rm cr}$ that represents the largest particle that is filled in with rime for a given F_r. The dimension $D_{\rm cr}$ partitions graupel and partially rimed crystals as indicated in Fig. 2; $D_{\rm cr}$ is found by calculating D such that at $D = D_{\rm cr}$, $m_r = m_g$. Equating m_r and m_g using (15) and (16) gives

$$D_{\rm cr} = \left[\left(\frac{1}{1 - F_r} \right) \frac{\alpha_i}{a_g} \right]^{1/(\beta_g - \beta_i)}. \tag{18}$$

For the selected set of m–D coefficients (see Table 1), $D_{\rm cr} \approx 800$ μm for $F_r = 0.75$. Note that if $F_r \to 1$, $D_{\rm cr} \to \infty$. In this case in the code $D_{\rm cr}$ is not calculated and the m–D and A–D relationships for the rimed crystals follow that of graupel.

The empirical m–D relationship for graupel applies to a limited size range. Extrapolation to smaller sizes gives a particle mass smaller than the corresponding value using the formulation for unrimed nonspherical ice. Thus, extrapolation leads to a bulk density of graupel that is smaller than that of unrimed ice for small particles. To avoid this inconsistency, the bulk density of graupel is assumed to always be greater than or equal to the bulk density of unrimed ice. These considerations lead us to define a second critical dimension, $D_{\rm gr}$, that represents the size where the bulk densities of unrimed ice and graupel are equal. Particles smaller than $D_{\rm gr}$ are assumed to have m–D relationship for unrimed ice, even though they may be rimed, to avoid unrealistically low bulk particle densities using the extrapolated m–D formulation for graupel. These particles are referred to as "dense nonspherical ice." Thus, $D_{\rm gr}$ partitions between dense nonspherical ice and graupel as indicated in Fig. 2. $D_{\rm gr}$ is derived assuming $m_g = m_i$. Using (16) and (10) gives

$$D_{\rm gr} = \left(\frac{\alpha_i}{\alpha_g} \right)^{1/(\beta_g - \beta_i)}. \tag{19}$$

For the selected set of m–D coefficients (see Table 1), $D_{\rm gr} \approx 120$ μm. Note that presence of dense nonspherical ice can also be thought as a way of representing inability of small ice crystals to grow by riming [see Eq. (23) and following discussion]. Since this partitioning between graupel and dense nonspherical ice is applied to both m–D and A–D, there is a small discontinuity in projected area between the two ice types at $D_{\rm gr}$. However, for the m–D and A–D values used here, this difference is only 0.8%. Particles with $D < D_{\rm th}$ have m–D and A–D relationships corresponding to solid ice spheres as in the case with no riming. Thus, $D_{\rm th}$ partitions between solid ice spheres and dense nonspherical ice as indicated in Fig. 2, in the same way as in the case with no riming.

To summarize the case with riming (i.e., when $F_r > 0$), the m–D and A–D relationships are found by dividing the PSD into four regions based on $D_{\rm th}$, $D_{\rm gr}$, and $D_{\rm cr}$: 1) particles with $D < D_{\rm th}$ follow m–D and A–D for solid ice spheres, 2) particles with $D_{\rm th} \le D < D_{\rm gr}$ follow m–D and A–D for nonspherical unrimed ice, 3) particles with $D_{\rm gr} \le D < D_{\rm cr}$ follow m–D and A–D for graupel, and 4) particles with $D \ge D_{\rm cr}$ follow m–D and A–D for partially rimed crystals. In the case of $F_r \approx 1$, all particles with $D > D_{\rm gr}$ follow m–D and A–D for graupel. Note that using $F_r = 0$ in the above equations for m–D and A–D for the case with riming is mathematically identical to the equations for the case with no riming. The key point is that this approach allows the m–D relationship to vary smoothly between solid ice spheres, dense nonspherical ice, graupel, and partially rimed crystals, for arbitrary F_r. Thus, key parameters such as mean particle fall speed vary smoothly between small and large unrimed crystals and between

unrimed and rimed crystals. An example of the variation of mass-weighted mean terminal fall speed as a function of the rime mass fraction is shown in Fig. 3. This plot shows a slow increase of V_q with F_r for F_r between 0 and 0.3 and a much more rapid increase for F_r between 0.6 and 1. The calculation of terminal particle fall speed is described more in the appendix.

With the m–D relationships established for different regions of the ice PSD for either $F_r = 0$ or $F_r > 0$, the size distribution parameters can be derived from (5)–(7). Because the ice PSD is divided into separate regions in terms of m–D, the integral (7) involves incomplete gamma functions; hence derivation of λ and N_0 from μ, q, and N cannot be done analytically as is the case for cloud droplets and rain. Instead, these parameters are calculated by iteration. Because this method is computationally inefficient, we use a lookup table approach that gives λ and N_0 as a function of the predicted ice variables q_{dep}, q_{rim}, and N. These parameters (along with the m–D and A–D relationships for each region of the PSD) are used to calculate the ice microphysical process rates in (1)–(3) as described in the appendix.

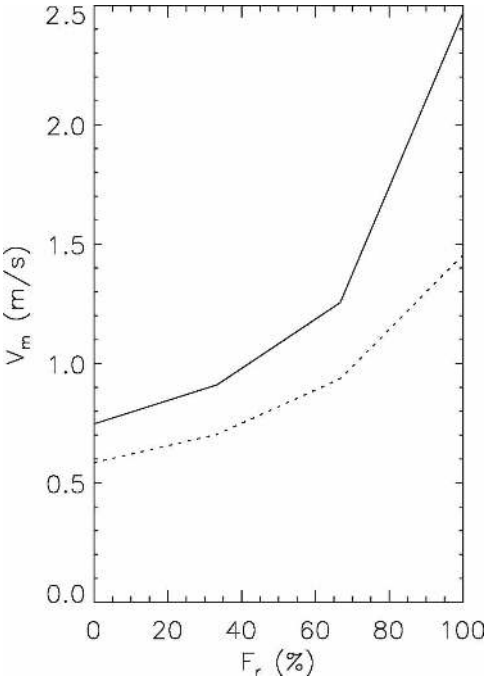

FIG. 3. Mass-weighted terminal fall speed V_m as a function of crystal rimed mass fraction F_r assuming pressure of 600 mb, temperature of 253 K, and total ice mixing ratio and ice number concentration of 1 g kg^{-1} and 3 L^{-1} (solid) or 0.1 g kg^{-1} and 3 L^{-1} (dotted).

3. Description of the kinematic framework and case study

The bulk model with the new ice microphysics scheme was implemented in a 2D kinematic modeling framework similar to that presented by Szumowski et al. (1998) and subsequently applied in Grabowski (1998, 1999) and MG07. The kinematic framework employs a specified flow field, which allows for testing of the microphysics scheme in a framework that includes advective transport and particle sedimentation while at the same time avoiding complications due to feedbacks between the dynamics and microphysics. In addition to the equations describing conservation of the mixing ratios and number concentrations of ice, cloud droplets, and rain, the kinematic model solves equations for the potential temperature and water vapor mixing ratio. These equations include advective transport and sinks/sources due to condensation/evaporation and latent heating. Transport in physical space is calculated using the 2D version of the multidimensional positive definite advection transport algorithm (MPDATA) scheme (Smolarkiewicz 1984; Smolarkiewicz and Margolin 1998). The vertical and horizontal grid spacing is 50 m over a domain 9 km wide and 3 km deep; the model time step is 0.5 s

The specified flow field varies in time, representing the evolution of an idealized shallow convective plume. The flow pattern consists of low-level convergence, upper-level divergence, and a narrow updraft at the center of the domain. Horizontal flow includes a weak vertical shear. Equations describing the streamfunction and flow velocities are detailed in the appendix of MG07. Here the updraft decays to zero velocity after 40 min instead of 2 m s^{-1} in MG07, which allows slower-falling ice and graupel (relative to rain) to fall toward the surface. In addition, two flow configurations are tested, corresponding with a maximum updraft speed of either 2 or 8 m s^{-1} (MG07 used 8 m s^{-1} only). This allows for testing of the scheme in both weak updraft (and low supercooled liquid water) and moderate updraft (high supercooled liquid water) environments. The updraft speed is held constant at 1 m s^{-1} for the first 15 min, intensifies to a peak value of either 2 or 8 m s^{-1} at 25 min, and decays to zero after 40 min (Fig. 4). The simulated time period is from $t = 0$ to 90 min.

This case, detailed by Szumowski et al. (1998), was originally developed for warm conditions. Here, we reduce the initial temperature profile of Szumowski et al. by 20 K to simulate mixed-phase conditions in a cold cumulus. The cloud-top temperature is about 258 K, with temperatures above freezing in the lowest 500 m (Fig. 5). The initial water vapor mixing ratio is also reduced such that the initial relative humidity is the same as in Szumowski et al. Following Szumowski et al.

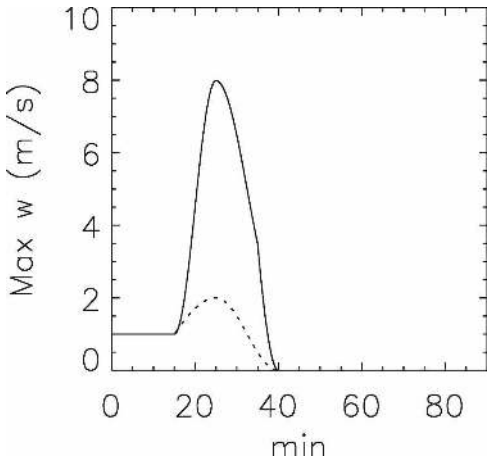

FIG. 4. Maximum updraft velocity w in the X–Z plane as a function of time for peak updraft strength of 8 (solid) and 2 m s^{-1} (dotted).

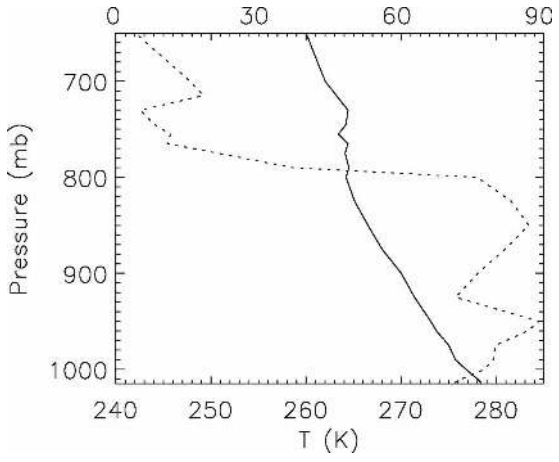

FIG. 5. Initial temperature T (solid) and relative humidity (RH) (dotted) profiles.

and MG07, entrainment and subgrid turbulent mixing are neglected.

Droplet activation is calculated from the water supersaturation and specified aerosol characteristics using Kohler theory (see MG07, section 2 for details). A single lognormal aerosol size distribution is assumed. Here, we assume a moderately polluted regime with a total concentration of accumulation mode aerosol of 300 cm^{-3}. The other aerosol characteristics (composition, mean size, standard deviation of size) are the same as MG07 (see their section 3 for details).

To test the new approach for ice microphysics (hereafter referred to as the "new scheme"), we have also developed a version of the scheme that uses the traditional approach for conversion of ice/snow to graupel following Rutledge and Hobbs (1984; hereafter RH84); hereafter, this version is referred to as the "traditional scheme." In this scheme there are four prognostic ice variables: ice/snow mixing ratio and number concentration, and graupel mixing ratio and number concentration. Note that this scheme does not include separate variables for cloud ice and snow as in most bulk schemes, and therefore does not use the autoconversion process to convert small to large ice particles. Several processes convert ice/snow to graupel following RH84. These include graupel initiation from both rain–snow and droplet–snow collisions. All other microphysical processes are calculated in the same manner as in the new scheme, assuming that $F_r = 0$ for ice/snow and $F_r = 1$ for graupel. The minimum mixing ratios required to initiate graupel from rain–snow collisions are 0.1 g kg^{-1} for both rain and ice/snow following RH84. For graupel initiation resulting from snow–droplet collisions, a minimum snow mixing ratio of 0.1 g kg^{-1} and minimum droplet mixing ratio of 0.5 g kg^{-1} are required following RH84. If the graupel initiation conditions are met, it is assumed that all rain–snow and droplet–snow collisions result in conversion to graupel. The sensitivity of the traditional scheme to these threshold mixing ratios is described in section 4b. Note that RH84 also included graupel initiation due to collisions between cloud ice and rain; this is neglected here because we do not include separate variables for cloud ice and snow.

4. Results

a. Baseline simulations

We first focus on the shallow cumulus simulations with a maximum updraft speed of 8 m s^{-1} using either the new scheme or the traditional scheme for ice microphysics. The time–height plots of maximum values of cloud water, rain, ice/snow, and/or graupel mixing ratios are shown in Figs. 6 and 7. These plots are created by combining, at a given time, the horizontal maximum of a given field at each model vertical level into a single column and subsequently displaying the time evolution of these columns. Hence, these plots trace vertical movement of the horizontal field maxima, but no information about their horizontal location is available. Moreover, the time evolution of the domain-average cloud liquid water path (LWP), ice water path (IWP), water optical depth τ_c, ice cloud optical depth τ_i, total cloud optical depth $\tau_t = \tau_c + \tau_i$, and the surface precipitation rate (PREC) are all shown in Fig. 8. The cloud droplet optical depth is calculated as $\tau_c = \int_0^H 3\mathrm{LWC}/(2\rho_w r_e)\, dz$ for the geometric optics limit, where H is the top of the model domain, LWC is the

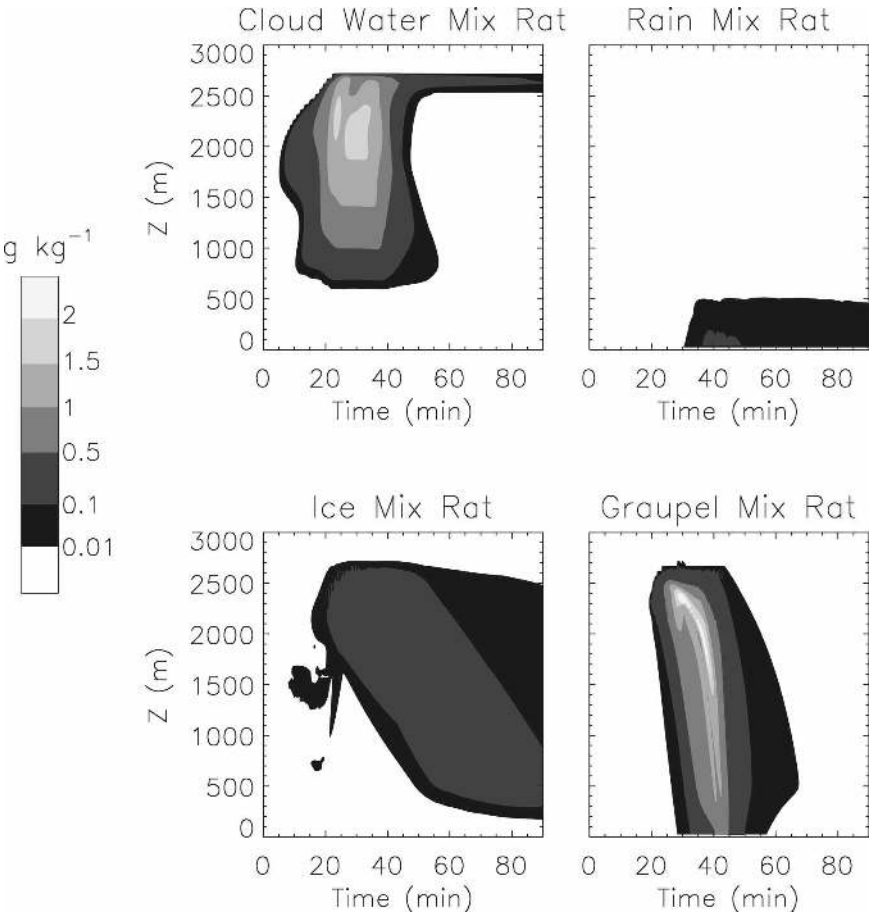

FIG. 6. Time evolution of horizontal maxima of cloud water mixing ratio, rain mixing ratio, ice/snow mixing ratio, and graupel mixing ratio at each vertical level using the traditional scheme and maximum updraft speed of 8 m s^{-1}.

liquid water content, and r_e is the droplet effective radius, calculated as the ratio of the third and second moments of the gamma droplet size distribution (MG07). For ice, calculation of the optical depth is complicated by the nonspherical geometry of ice crystals. Here we employ the parameterization of Fu (1996), which derives the effective ice diameter as

$$D_e = 2\sqrt{3}\mathrm{IWC}/(3\rho_i A_c), \quad (20)$$

where A_c is the projected area of the crystals from the given A–D relationship (see section 2) integrated over the size distribution, and IWC is the ice water content. The Fu (1996) optical depth at ~0.6 μm (wavelength of maximum solar irradiance) is

$$\tau_i = \int_0^H \mathrm{IWC}(0.000\,982\,244 + 2.508\,75/D_e)\,dz, \quad (21)$$

where IWC has units of g m^{-3} and D_e has units of μm.

As Figs. 6 and 7 show, model results are generally similar when using either scheme, but there are significant differences. The cloud water is produced in both simulations as the updraft increases in strength between $t = 0$ and 25 min. Significant amounts of ice are produced by the time of the maximum updraft ($t = 25$ min) through deposition/condensation–freezing nucleation as well as droplet freezing. The noisy pattern seen in the ice and graupel mixing ratios using the traditional scheme in Fig. 6 likely reflects the thresholding behavior of graupel conversion. As the updraft weakens after $t = 25$ min, a shaft of ice precipitation develops and partially melts near the surface. The cloud water is rapidly glaciated throughout most of the cloud layer, except near cloud top owing to limited amounts of ice in this region. The separation of ice/snow and graupel into different categories using the traditional approach produces two shafts of ice precipitation and associated maxima of surface precipitation rate consisting of either graupel or ice/snow (see Fig. 8). Since the traditional approach converts ice/snow to graupel in a single step,

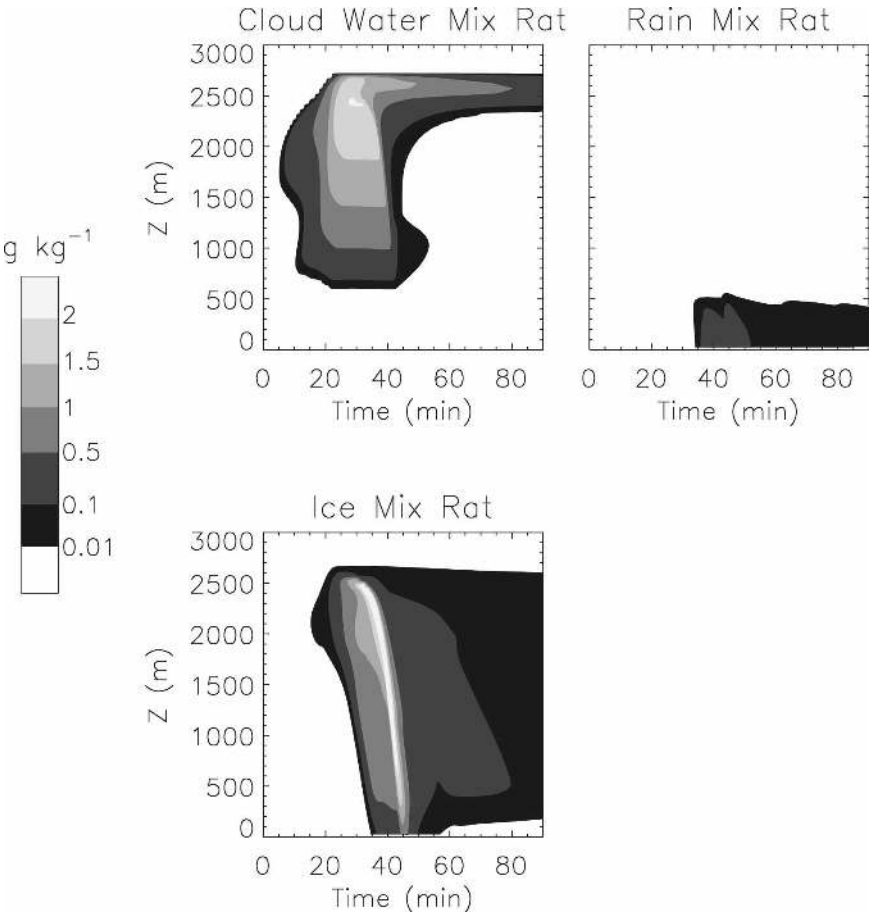

FIG. 7. Time evolution of horizontal maxima of cloud water mixing ratio, rain mixing ratio, and ice mixing ratio at each vertical level using the new scheme and maximum updraft speed of 8 m s^{-1}.

rapid conversion to graupel occurs once the threshold conditions are met, and this shaft of graupel precipitates rapidly to the surface with mean fall speeds greater than 1.5 m s^{-1}. Significant surface precipitation (consisting of both graupel and rain) begins at $t = 30$ min in this run and produces a sharp peak in the precipitation rate at $t = 40$ min (see Fig. 8). A secondary peak in the surface precipitation rate occurs at about $t = 80$ min associated with the weaker shaft of ice precipitation consisting of ice/snow. Because of the much slower particle fall speeds associated with the ice/snow category (about 0.5–1 m s^{-1}) relative to graupel, much of this shaft does not reach the surface by the end of the simulation at $t = 90$ min.

In contrast, the new scheme produces a single shaft of ice precipitation; its formation is also slightly delayed relative to the main precipitation shaft produced by the traditional scheme (see Fig. 8). Similarly to the traditional scheme, weak surface precipitation continues up to the end of the simulation, but in contrast there is no distinct second peak in precipitation rate. Ice mixing ratio is primarily grown by vapor deposition initially; rimed mass fraction exceeding 90% occurs 10–20 min after the first appearance of the ice (see Fig. 9). Rimed mass fraction steadily decreases after about $t = 45$ min corresponding to the reduction of droplet mixing ratio and hence decrease in the riming rate and accumulated rime mass. Most of the cloud layer has a crystal concentration between 1 and 5 L^{-1}. Allowing Hallett–Mossop rime splintering increases number concentration in the precipitation shaft up to about one order of magnitude (not shown). Since the shaft of ice precipitation consists of a mixture of partially rimed crystals and graupel, depending on the particle size (as described in section 2; see also Fig. 2), the mean particle fall speed is slightly less than that for a population consisting solely of graupel. Thus, this shaft of precipitation falls slower than the graupel shaft in the simulation using the traditional scheme, and significant precipitation does not reach the surface until about $t = 35$ min,

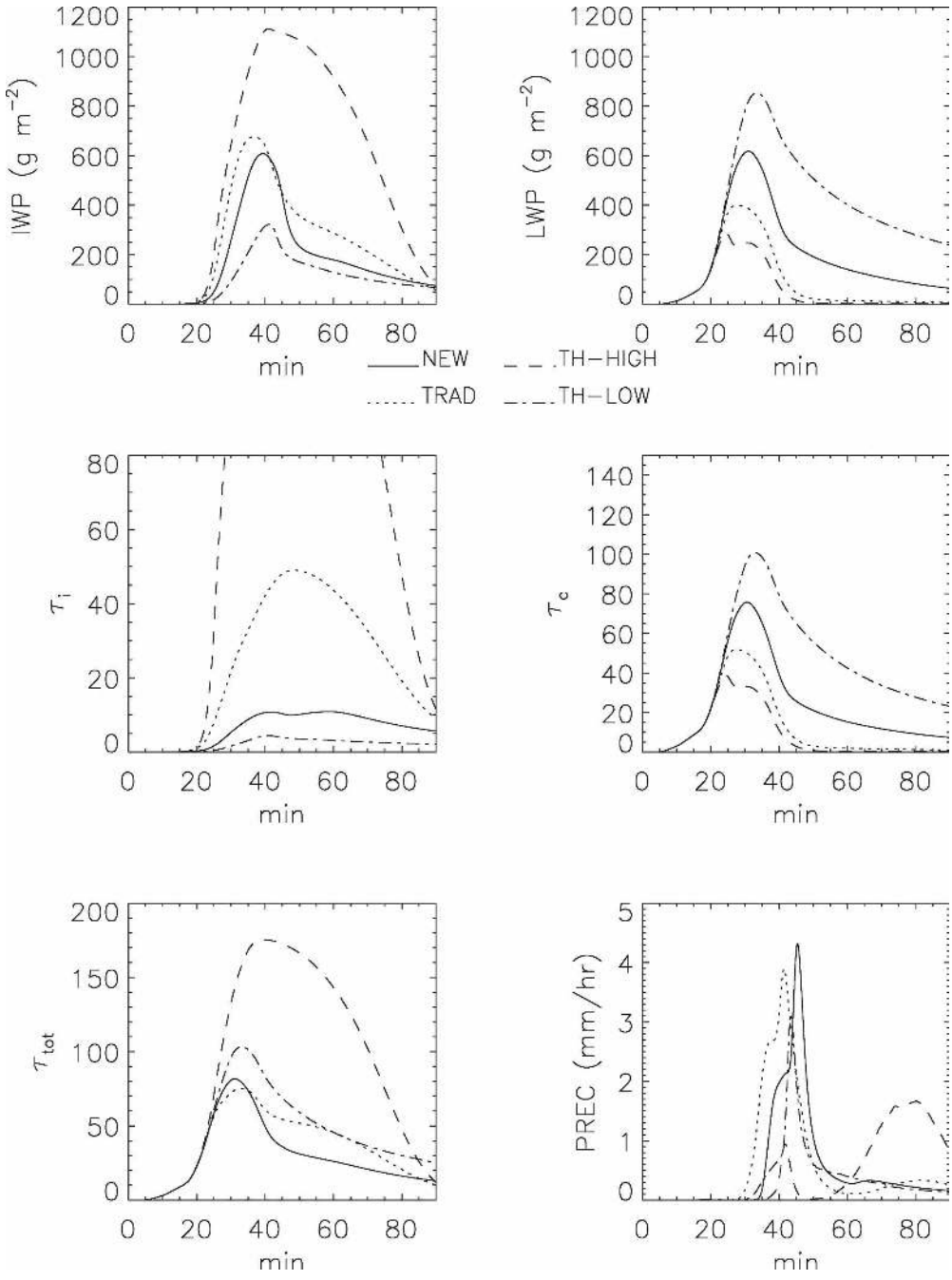

FIG. 8. Time evolution of domain-average cloud liquid water path (LWP) (g m^{-2}), ice water path (IWP) (g m^{-2}), droplet optical depth τ_c (unitless), ice optical depth τ_i (unitless), total cloud optical depth τ_{tot} (unitless), and surface precipitation rate PREC (mm h^{-1}) for maximum updraft speed of 8 m s^{-1}. NEW and TRAD refer to simulations using the new and traditional ice microphysics schemes, respectively. TH-HIGH and TH-LOW refer to sensitivity tests using the traditional scheme but with the threshold ice/snow and droplet mixing ratios for graupel production during droplet collection increased or decreased, respectively.

a delay of about 5 min compared to the run with the traditional scheme (see Fig. 8). The peak surface precipitation rate is similarly delayed by about 5 min. Moreover, the new scheme produces significantly more cloud liquid water than the traditional scheme, especially after $t = 45$ min. These differences are also evident for the time- and domain-average values of LWP, optical depths, and surface precipitation rate (Table 2).

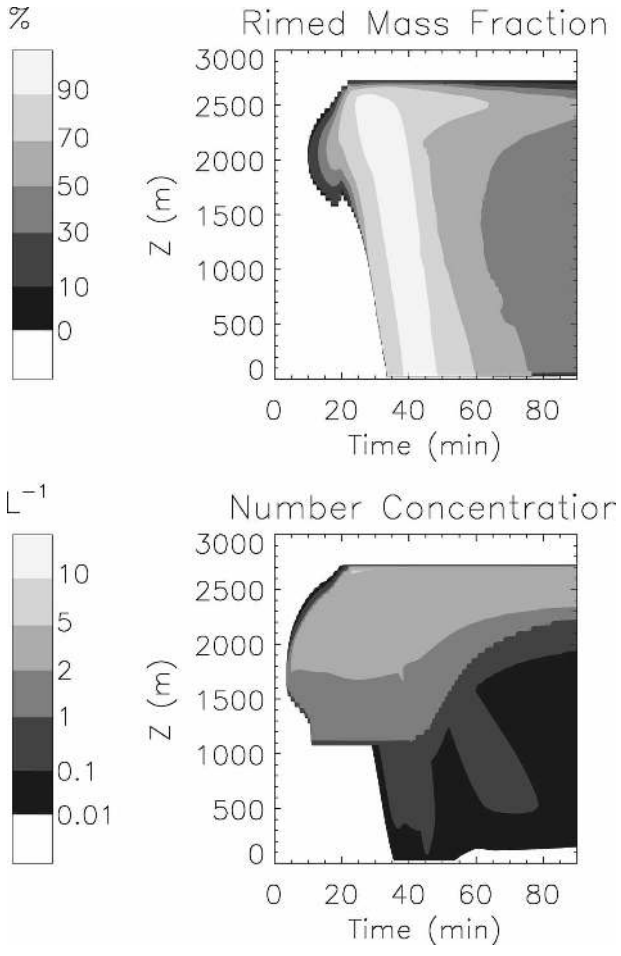

FIG. 9. (top) Time evolution of rimed mass fraction at the location of horizontal maximum ice mixing ratio at each vertical level and (bottom) time evolution of horizontal maximum ice number concentration at each vertical level, using the new scheme and maximum updraft speed of 8 m s^{-1}.

For ice optical depth, the difference is more significant, even though the ice water path is only somewhat smaller using the new scheme. This appears to reflect the fact that dense, heavily rimed crystals in the new scheme have a relatively large ratio of mass to projected area (i.e., larger effective radius) compared to the unrimed crystals in the traditional scheme. Similar differences are apparent for the simulations with maximum updraft velocity of 2 m s^{-1} (see Fig. 10 and Table 2).

b. *Sensitivity tests*

Simulations using the traditional scheme exhibit strong sensitivity to the assumed ice/snow and cloud water threshold mixing ratios required for conversion to graupel. Two tests demonstrate this sensitivity. In the first test, conversion to graupel during collection of droplets is allowed only when both the ice/snow and droplet mixing ratios exceed 1 g kg^{-1}, compared to thresholds of 0.1 and 0.5 g kg^{-1} for ice/snow and droplets, respectively, for the baseline run using the traditional scheme (as well as in RH84). In the second test, conversion to graupel during collection of droplets occurs when any ice/snow and droplet mixing ratio is present (i.e., thresholds are set to zero). Note that results are not sensitive to the mixing ratio thresholds for conversion to graupel during rain–snow collisions because the formation of graupel is dominated by collisions between ice/snow and cloud droplets. A similar result was noted by RH84 in simulations of cold-frontal rainbands.

As expected, increasing the threshold ice/snow and droplet mixing ratios to 1 g kg^{-1} decreases the amount of graupel. Since particles fall speeds for ice/snow are much slower than they are for graupel, ice mass is removed relatively slowly from the cloud. This leads to much larger values of IWP and rapid depletion of cloud liquid water through droplet collection and the diffusional growth of the ice field (see Figs. 8 and 10). It also leads to a smaller initial peak in the surface precipitation rate (at about t = 41 min) and much larger second peak (at t = 80 min) relative to the baseline run using the traditional scheme. Even though the LWP is small with the reduced graupel thresholds, the large IWP results in a total cloud optical depth about 3 times larger than baseline for maximum updraft velocity of 8 m s^{-1} (see Table 2). Ice optical depth is further enhanced relative to the baseline traditional simulation because most of the ice mass is contained in the unrimed ice/snow category, representing less dense crystals with a smaller ratio of mass to projected area (i.e., smaller effective radius) relative to graupel. Thus, partitioning between unrimed ice/snow and graupel can directly impact the radiative properties of the simulated cloud. Similar results are seen for the run with updraft velocity of 2 m s^{-1}. Not surprisingly, reducing the threshold mixing ratios for graupel production leads to an increase in the LWP and decrease in the IWP relative to baseline due to faster removal of cloud ice. Despite large changes in the ice and liquid water paths, the total cloud optical depth is similar to baseline. Thus, the traditional approach produces a larger total cloud optical depth than the new scheme regardless of values specified for the threshold mixing ratios for graupel production. This suggests that simple tuning of the threshold mixing ratios in the traditional approach will not be able to reproduce results using the new scheme; even if such tuning were possible, it would likely be case dependent.

The sensitivity to the specified m–D relationship for

TABLE 2. Time- and domain-average cloud liquid water path (LWP) (g m^{-2}), ice water path (IWP) (g m^{-2}), water optical depth τ_c (unitless), ice optical depth τ_i (unitless), total cloud optical depth τ_{tot} (unitless), and surface precipitation rate (PREC) (mm h^{-1}) for simulations with maximum updraft speed w of either 2 or 8 m s^{-1}. NEW and TRADITIONAL refer to simulations using the new and traditional ice microphysics schemes, respectively. TH-HIGH and TH-LOW refer to sensitivity tests using the traditional scheme but with the threshold ice/snow and droplet mixing ratios for graupel production during droplet collection increased or decreased, respectively (see text for details). S1 and H07 refer to sensitivity tests with the new scheme using the m–D relationship for side planes or from H07, respectively. The averaging period is from t = 25 to 90 min.

Run	Max w	LWP	IWP	τ_c	τ_i	τ_{tot}	PREC
NEW	8	228.4	237.1	26.7	8.6	35.3	0.68
TRADITIONAL	8	92.9	317.9	12.1	32.6	44.7	0.76
TH-HIGH	8	52.8	719.3	7.4	111.0	118.4	0.62
TH-LOW	8	474.7	137.5	52.6	2.8	55.4	0.46
S1	8	288.8	198.0	33.3	4.6	37.9	0.64
H07	8	477.0	136.5	52.1	2.4	54.5	0.52
NEW	2	49.8	85.3	7.1	4.5	11.6	0.23
TRADITIONAL	2	16.8	140.4	2.7	20.9	23.6	0.20
TH-HIGH	2	15.4	169.4	2.5	26.4	28.9	0.20
TH-LOW	2	122.8	34.3	16.0	0.8	16.8	0.14

unrimed crystals is tested in the new scheme using the recent formulation derived by Heymsfield et al. (2007b; hereafter H07). Note that modifying this m–D relationship also impacts m–D for partially rimed crystals as indicated by (15), as well as the threshold dimensions delineating the size spectra illustrated in Figs. 1 and 2. The H07 formulation is based on crystal ensembles observed in convectively generated ice cloud layers during the 2002 Cirrus Regional Study of Tropical Anvil and Cirrus Layers-Florida Area Cirrus Experiment (CRYSTAL-FACE). The relationship is given by (cgs units) $m = (0.004\,015\,7 + 0.000\,060\,6\,T)\,D^{1.75}$, where T is the air temperature in degrees Celsius. Here we use $T = -5$°C; there is little change in our results over the range $-20 < T < -5$°C. An example of the sensitivity to habit is also tested using the m–D relationship for side planes following Mitchell et al. (1990), where $m = 0.004\,19\,D^{2.3}$ (cgs units; the baseline simulation assumes plates with sectorlike branches). Side planes may be expected in water saturated conditions as occur here, but at somewhat colder temperatures (from −20° to −25°C; Pruppacher and Klett 1997, and references therein). The impact of m–D relationship is mostly expressed through changes in the mean particle terminal fall speed. For a given set of ice conditions (i.e., mixing ratio and number concentration), the H07 formulation tends to produce larger mean fall speed (it should be kept in mind that the mean fall speed also depends on the A–D relationship, which was not varied in these tests). Thus, larger fall speed depletes the cloud of ice, reducing the IWP (and ice optical depth) and increasing the LWP (and droplet optical depth) (Fig. 11 and Table 2). There is little impact on the surface precipitation rate. This is because the surface precipitation (especially at the time of the peak rate) consists of ice with a high rimed mass fraction, which has microphysical characteristics closer to graupel than unrimed ice. It is anticipated that the surface precipitation rate will be more sensitive in conditions that lead to less riming. Using the m–D relationship for side planes produces only small changes in the results, leading to slight reduction in ice optical depth that is compensated by a slight increase in droplet optical depth (see Fig. 11).

To summarize the above sensitivity tests, it appears that the new scheme shows some sensitivity to the formulation of the m–D relationship for ice particles. However, this sensitivity appears to be significantly smaller than the impact of the conversion thresholds in the traditional scheme (see Figs. 8 and 10; Table 2).

5. Summary and conclusions

This paper documents a novel approach for representing the ice-phase microphysics in numerical models. It includes only a single species of ice but retains the history of rimed mass fraction, in contrast to the traditional approach of separating ice into several distinct categories (e.g., cloud ice, snow, graupel). The new approach allows for a physically based representation of the conversion of cloud ice into snow due to diffusional growth and aggregation, and the conversion of cloud ice and snow into graupel due to riming. The conceptual model of Heymsfield (1982) is applied for the latter. The history of rimed mass fraction in the new scheme is retained by predicting two ice mixing ratio variables: the mixing ratio acquired through water vapor deposition and the mixing ratio acquired through riming. Concentration of ice particles is the third predicted variable. All ice microphysical processes and parameters are calculated in a self-consistent manner us-

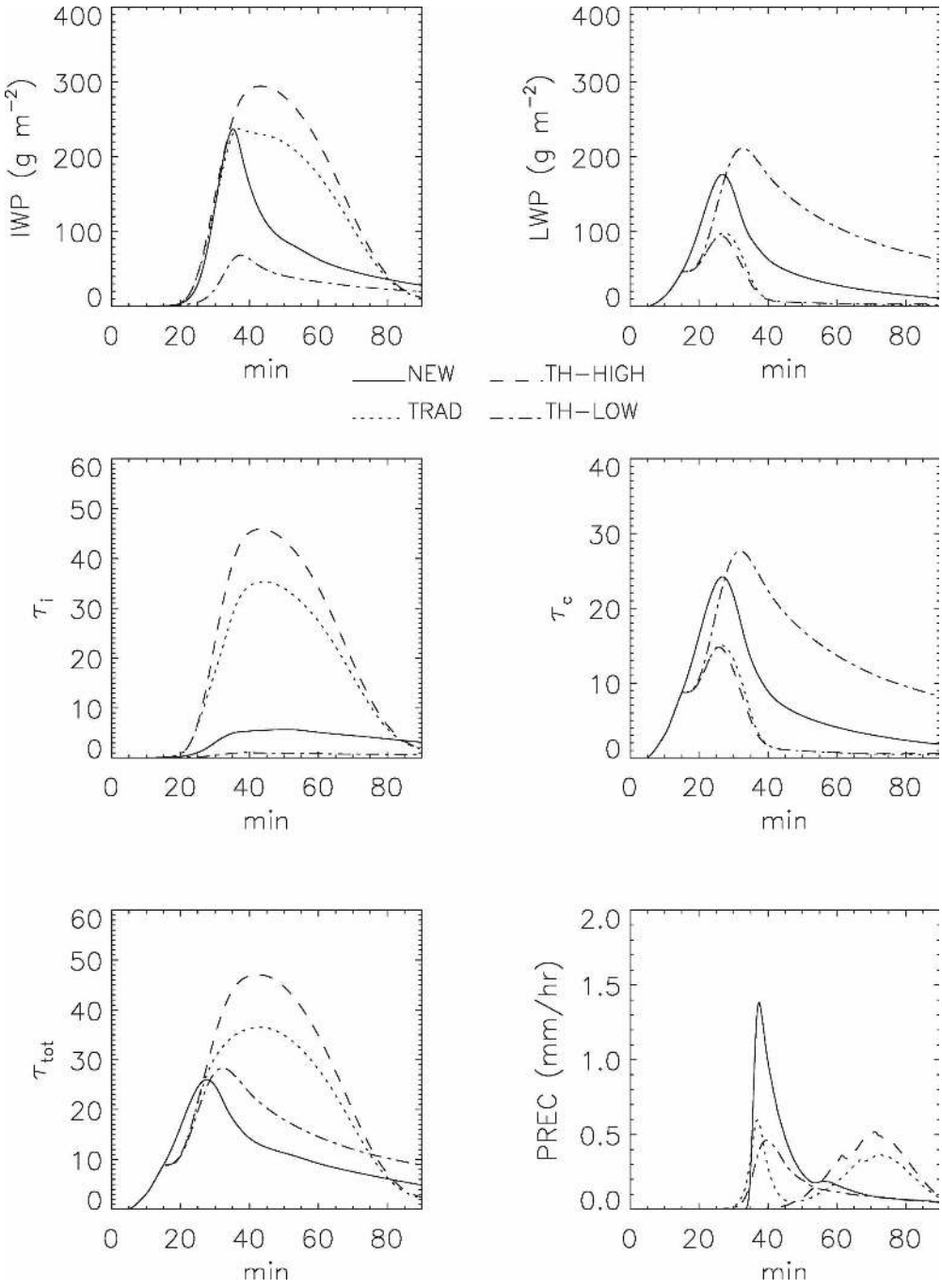

FIG. 10. As in Fig. 7 except for maximum updraft speed of 2 m s^{-1}.

ing mass–dimension (m–D) and projected-area–dimension (A–D) relationships that vary according to the rimed mass fraction and the particle size. Because the new approach does not include separate categories for small cloud ice, snow, and graupel, the nonphysical conversion processes are not needed, in contrast to traditional approaches. In the new scheme, the distinction between small ice and larger snow crystals, and between unrimed and rimed ice particles, is made by assuming a smooth transition in the m–D and A–D relationships for particles of different sizes and different rimed mass fractions. Another advantage of the new approach is that there are fewer prognostic variables, reducing the computational cost relative to traditional

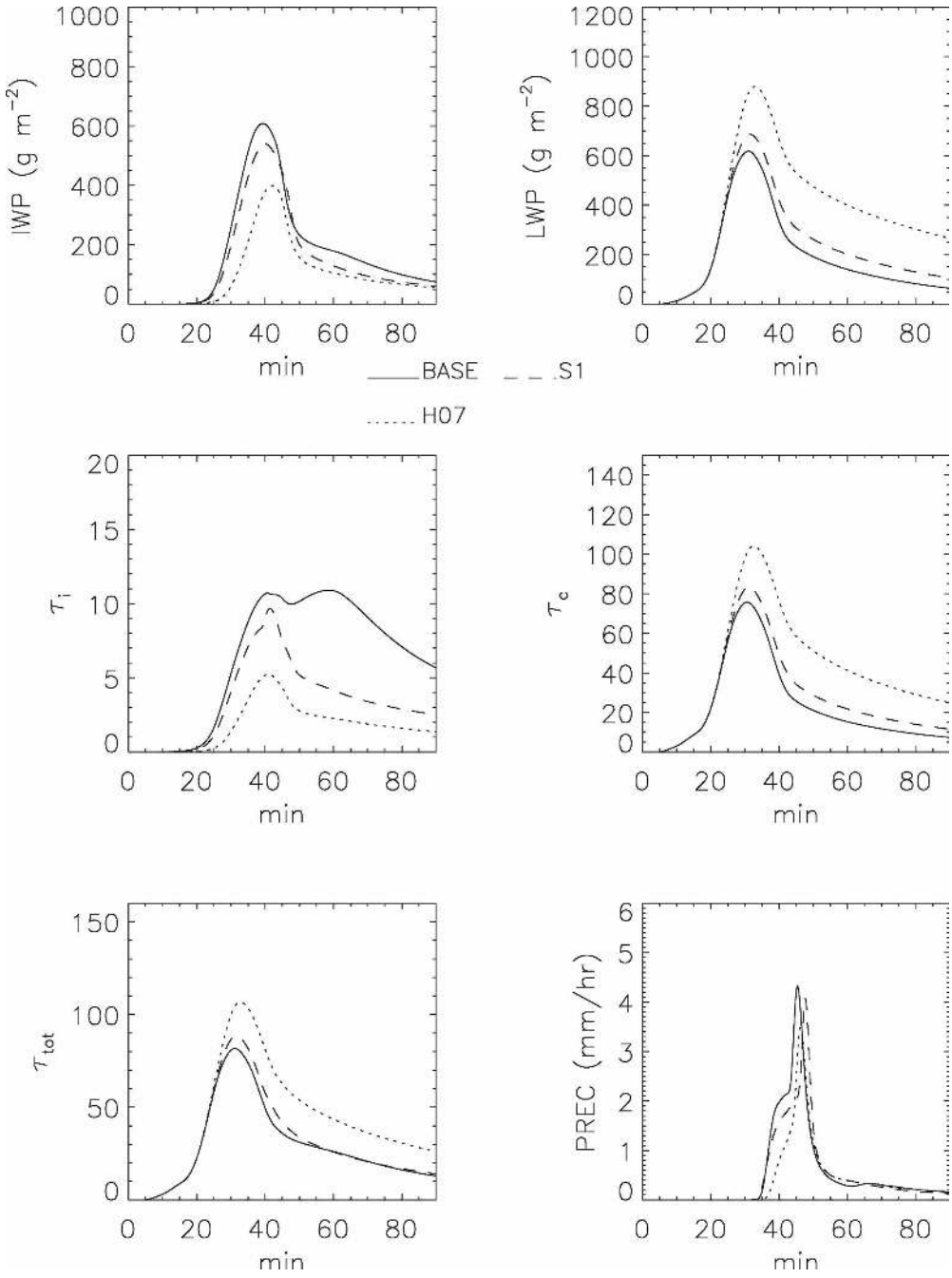

FIG. 11. Time evolution of domain-average cloud liquid water path (LWP) (g m^{-2}), ice water path (IWP) (g m^{-2}), droplet optical depth τ_c (unitless), ice optical depth τ_i (unitless), total cloud optical depth τ_{tot} (unitless), and surface precipitation rate (PREC) (mm h^{-1}) for maximum updraft speed of 8 m s^{-1}. BASE refers to the baseline simulation using the new scheme; S1 and H07 refer sensitivity tests using the new scheme with the crystal mass–dimension relationship for side planes and crystal ensembles following H07, respectively.

approaches. This strategy can be applied in either bulk or bin microphysical models. Application of the new approach to a bin model is currently underway; this work will be reported in a future publication.

A key aspect of the scheme is its flexibility: the scheme could be easily modified to account, for example, for crystals that form under varying environmental conditions with different habits and subse-

quently mix together. This could be accomplished by adding additional "classes" of ice with different m–D and A–D relationships for the different habits, and predicting three variables (the two mixing ratio variables plus number concentration) for each class. The scheme currently assumes riming growth in the dry growth regime (i.e., accreted drops are assumed to freeze instantaneously), but could also be modified to account for wet growth (i.e., riming when liquid water accumulates on the ice particle surface) by predicting the liquid water fraction accumulated on the particle and accounting for shedding. This is especially important for initiation of hail (Heymsfield and Hjelmfelt 1984). The new approach assumes that the rimed mass fraction is constant with particle dimension (for crystals larger than the riming threshold size) based on a simple scaling argument of the riming growth rate as a function of particle size. This assumption will be tested more rigorously using a bin model approach that explicitly predicts the evolution of rimed mass fraction with particle size; results will be reported in a future publication. The approach developed in this paper could be easily modified to account for a rimed mass fraction that varies with ice particle size.

Here the new ice scheme was combined with the two-moment bulk microphysical framework of Morrison and Grabowski (MG07). In addition to four prognostic variables describing warm-rain processes (mixing ratios and number concentrations for cloud droplets and drizzle/rain), three prognostic variables were applied for ice processes (i.e., concentration of ice particles and the mixing ratios due to vapor depostion and riming). The scheme was applied in a 2D kinematic modeling framework mimicking a mixed-phase shallow cumulus with a maximum updraft speed of either 2 or 8 m s^{-1}. The new scheme was compared against a version that included the traditional approach for graupel conversion processes following RH84. Significant differences were apparent between the new and traditional approaches. In particular, the traditional approach with threshold mixing ratios prescribed as in RH84 produced two precipitation shafts and maxima of surface precipitation rate (separated by about 40 min) corresponding with either the graupel or ice/snow categories (and their attendant differences in particle fall speed). In contrast, the new scheme produced a single precipitation shaft. In addition, the new scheme produced more liquid water and less ice, and smaller (by about 20%–50%) mean total (ice plus liquid) cloud optical depth.

In the traditional approach, threshold mixing ratios must be reached before graupel production is allowed during riming. The values specified for these thresholds are arbitrary and have little physical basis. The traditional scheme exhibited strong sensitivity to these thresholds. Similarly to the findings of RH84, increasing the mixing ratio thresholds limited graupel formation, which in turn reduced the mean fall speed and altered the characteristics of the surface precipitation. In our study, precipitation was enhanced toward the end of the simulation. In addition, the slower mean fall speed led to the larger amounts of ice in the cloud layer, which rapidly depleted the available liquid water. Conversely, decreasing the mixing ratio thresholds for graupel formation increased graupel production and, hence, mean fall speed. This led to much smaller amounts of ice and hence larger liquid water path. Changing graupel thresholds also directly impacted ice optical depth since unrimed crystals have a smaller ratio of mass to projected area (i.e., smaller effective radius) compared to graupel. A key point is that the new approach does not require these arbitrary thresholds for graupel conversion.

The sensitivity to specified crystal mass–dimension relationship was also tested using the recent formulation developed by Heymsfield et al. (H07) from observations of crystal ensembles during CRYSTAL-FACE. The sensitivity was also tested using the mass–dimension relationship for side planes (the baseline simulation assumed plates with sectorlike branches). The impact of mass–dimension relationship occurred mostly through changes in the particle fall speed. For example, using the H07 formulation tended to increase the mean fall speed relative to baseline, resulting in smaller ice water path and larger liquid water path. There was little impact on the surface precipitation, but greater sensitivity is expected for cases that exhibit less riming. Note that using a mass–dimension relationship obtained from crystal ensembles (as in H07), rather than a specific crystal habit, is perhaps more justified since most clouds containing ice consist of a population of different habits including regular and irregular crystals, aggregates, broken branches, and polycrystals (e.g., Korolev et al. 1999; Heymsfield 2003). However, it is noted that ensemble characteristics vary widely between different regimes, such as synoptic versus convectively generated cirrus (H07).

In the future we will focus on testing the scheme within a 3D dynamic framework over a range of different conditions (e.g., deep convection, synoptic cirrus, mixed-phase stratocumulus), including comparison with observations, as well as looking at the impact of ice microphysics on the cloud dynamics, which could not be investigated using the kinematic framework employed in this study. Results of such investigations will be reported in future publications.

Acknowledgments. This work was supported by the NOAA Grant NA05OAR4310107 (W. Grabowski, PI) and by the NSF Science and Technology Center for Multi-Scale Modeling of Atmospheric Processes (CMMAP), managed by Colorado State University under Cooperative Agreement ATM-0425247. Comments on the manuscript by P. Field and R. Rasmussen are appreciated. We also thank A. Heymsfield for helpful discussions.

APPENDIX

Ice Microphysical Processes

a. Primary and secondary ice initiation

The number of ice nuclei acting in deposition and condensation freezing nucleation modes on insoluble or partially soluble aerosol (but not activated as cloud or rain drops), $N_{\rm IN}$, is given by Meyers et al. (1992) as a function of ice supersaturation. Nucleation is allowed in conditions with 5% or greater ice supersaturation at temperatures less than 268.15 K. The initial radius of a new crystal is 1 μm. At present we assume that ice nuclei are always available (ice nuclei concentration is not predicted), so that

$$\left(\frac{\partial N}{\partial t}\right)_{\rm nuc} = \frac{N_{\rm IN} - N}{\Delta t}, \tag{A1}$$

where N is the number concentration of existing ice and Δt is the time step. Ice supersaturation is calculated from the predicted temperature and water vapor mixing ratio fields.

The freezing of rain and cloud droplets occurs through immersion mode following Bigg (1953) and contact mode following Young (1974). The number concentration of ice nuclei acting in contact mode is given by Meyers et al. (1992) as a function of temperature. Contact and immersion freezing rates are dependent on the droplet size and hence are integrated over the droplet and rain size distributions. Ice multiplication occurs by rime splintering following Hallett and Mossop (1974). However, for cleaner comparison with the traditional approach to ice microphysics, rime splintering is turned off for the simulations shown here (this keeps particle number concentration fairly consistent between the various runs). At temperatures below -40°C, rain and cloud droplets freeze homogeneously within a single model time step.

b. Terminal fall velocity

The number- and mass-weighted terminal fall speeds V_N and V_q are found by integrating the particle fall speed across the size distribution with appropriate weighting by number of mass. The fall speed–dimension relationship (V–D) is given by the power law $V = a_1 D^{b_1}$. Here a_1 and b_1 are derived following Mitchell and Heymsfield (2005) from the R_e–X relationship, where X is the Best (Davies) number (related to mass divided by projected area of the particle) and R_e is the particle Reynolds number. This approach follows the methodology of Khvorostyanov and Curry (2002) to produce smooth coefficients a_1 and b_1 as a function of D, but modified to account for surface roughness coefficients appropriate for ice particles. The mass and projected area needed to calculate X are found from the m–D and A–D relationships as described in the previous subsection. The air density correction factor follows Heymsfield et al. (2007a). Since rimed mass fraction is assumed to be independent of D, the same mass-weighted terminal fall speeds are applied to both $q_{\rm dep}$ and $q_{\rm rim}$.

c. Collisions between ice and rain/cloud droplets

The formulation for collection of cloud water assumes that the fall speed of droplets is negligible compared to the collecting ice particles. Thus, the collection of cloud water is given by the continuous collection (e.g., Pruppacher and Klett 1997). Here it is assumed that the collection efficiency for droplet–ice collisions is 0.75 and the minimum crystal size for riming, $D_{\rm rim}$, is 100 μm. The bulk efficiency should depend on the mean size of cloud droplets (and to some extent on the crystal size, for crystals larger than $D_{\rm rim}$), an effect neglected in the current study [see Borys et al. (2003) for a discussion of how this effect impacts the growth of snow in cold orographic clouds]. As far as $D_{\rm rim}$ is concerned, previous studies have suggested that it is approximately between 50 and 300 μm depending on the particle habit (Pruppacher and Klett 1997, and references therein). For simplicity it is assumed that ice collects cloud water at subfreezing temperatures only. The collection of drizzle/rain drops by ice is similarly given by continuous collection, except that the fall speed of drizzle/rain is included since it is comparable (or greater) in magnitude to the ice particle fall speed. Note that there is no assumed minimum crystal size for the collection of small ice particles by drizzle/rain. At subfreezing temperatures, collisions between ice and drizzle/rain are assumed to result in instantaneous freezing of the liquid. At temperatures above freezing, these collisions are assumed to result in instantaneous melting of the ice.

d. Aggregation of ice crystals

The self-aggregation of ice through ice–ice collisions impacts N but not mixing ratio. The change in N due to self-aggregation is calculated by the continuous collection equation, with an assumed collection efficiency of

0.1 following Reisner et al. (1998). Field et al. (2006) found that using a sweep-out collection kernel with aggregation efficiency of about 0.1 was able to produce reasonable agreement with the observed evolution of the particle size distribution in anvil cirrus, although we note that collection efficiency may differ under varying environmental conditions (e.g., Mitchell 1988). Snow breakup is implicit by limiting the mean ice particle size to 5 mm (through adjustment of N) as described in section 2.

e. Vapor deposition/sublimation and melting

The vapor deposition growth, sublimation, and melting of ice is given by diffusional mass and heat balance neglecting surface kinetic effects but including ventilation effects (e.g., Pruppacher and Klett 1997). The ventilation coefficient is modeled after Hall and Pruppacher (1976) for $X > 1$, where $X(D) = N_{\rm Sc}^{1/3} N_{\rm Re}^{1/2}$, $N_{\rm Sc}$ and $N_{\rm Re}(D)$ are the Schmidt and Reynolds numbers associated with the falling particle for the given environmental conditions, respectively. The air density correction to the fall speed is neglected for $N_{\rm Re}$. Ventilation effects are neglected for $X(D) < 1$. The capacitance of the particles $C(D)$ varies for the different regions of the PSD in Fig. 1b. For ice spheres $C = D$. In the absence of empirical data, we also assume that $C = D$ for graupel. For unrimed nonspherical crystals the capacitance is given by Field et al. (2008): $C = 0.48D$. For partially rimed crystals, capacitance is found by linear interpolation between the values for unrimed crystals and graupel based on particle mass for a given D. The change in $q_{\rm dep}$ and $q_{\rm rim}$ due to melting and sublimation is partitioned based on their relative contributions to the total ice mixing ratio. Although N is not impacted by depositional growth, it is potentially reduced by sublimation and melting. For simplicity, the relative loss of N during sublimation and melting is equal to the relative loss of total ice mixing ratio following Ferrier (1994) and Morrison et al. (2005).

REFERENCES

Bailey, M., and J. Hallett, 2002: Nucleation effects on the habit of vapour grown ice crystals from −18 to −42°C. *Quart. J. Roy. Meteor. Soc.,* **128,** 1461–1483.

Berry, E. X., and R. L. Reinhardt, 1973: Modeling of condensation and collection within clouds. University of Nevada, Desert Research Institute Tech. Rep. Physical Sciences Publication 16, 96 pp.

Bigg, E. K., 1953: The supercooling of water. *Proc. Phys. Soc. London,* **66B,** 688–694.

Borys, R. D., D. H. Lowenthal, S. A. Cohn, and W. O. J. Brown, 2003: Mountaintop and radar measurements of anthropogenic aerosol effects on snow growth and snowfall rate. *Geophys. Res. Lett.,* **30,** 1538, doi:10.1029/2002GL016855.

Chen, J.-P., and D. Lamb, 1994: The theoretical basis for the parameterization of ice crystal habits: Growth by vapor deposition. *J. Atmos. Sci.,* **51,** 1206–1221.

Cober, S. G., and R. List, 1993: Measurements of the heat and mass transfer parameters characterizing conical graupel growth. *J. Atmos. Sci.,* **50,** 1591–1609.

Dudhia, J., 1989: Numerical study of convection observed during the Winter Monsoon Experiment using a mesoscale two-dimensional model. *J. Atmos. Sci.,* **46,** 3077–3107.

Ferrier, B. S., 1994: A double-moment multiple-phase four-class bulk ice scheme. Part I: Description. *J. Atmos. Sci.,* **51,** 249–280.

Field, P. R., A. J. Heymsfield, and A. Bansemer, 2006: A test of ice self-collection kernels using aircraft data. *J. Atmos. Sci.,* **63,** 651–666.

——, ——, ——, and C. H. Twohy, 2008: Determination of the combined ventilation factor and capacitance for ice crystal aggregates in airborne observations in a tropical anvil cloud. *J. Atmos. Sci.,* **65,** 376–391.

Fu, Q., 1996: An accurate parameterization of the solar radiative properties of cirrus clouds for climate models. *J. Climate,* **9,** 2058–2082.

Geresdi, I., 1998: Idealized simulation of the Colorado hailstorm case: Comparison of bulk and detailed microphysics. *Atmos. Res.,* **45,** 237–252.

Gilmore, M. S., J. M. Straka, and E. N. Rasmussen, 2004: Precipitation uncertainty due to variations in precipitation particle parameters within a simple microphysics scheme. *Mon. Wea. Rev.,* **132,** 2610–2627.

Grabowski, W. W., 1998: Toward cloud resolving modeling of large-scale tropical circulations: A simple cloud microphysics parameterization. *J. Atmos. Sci.,* **55,** 3283–3298.

——, 1999: A parameterization of cloud microphysics for long-term cloud-resolving modeling of tropical convection. *Atmos. Res.,* **52,** 17–41.

Gu, Y., and K. N. Liou, 2000: Interactions of radiation, microphysics, and turbulence in the evolution of cirrus clouds. *J. Atmos. Sci.,* **57,** 2463–2479.

Hall, W. D., and H. R. Pruppacher, 1976: The survival of ice particles falling from cirrus clouds in subsaturated air. *J. Atmos. Sci.,* **33,** 1995–2006.

Hallett, J., and S. C. Mossop, 1974: Production of secondary ice particles during the riming process. *Nature,* **249,** 26–28.

Hashino, T., and G. J. Tripoli, 2007: The Spectral Ice Habit Prediction System (SHIPS). Part I: Model description and simulation of the vapor deposition process. *J. Atmos. Sci.,* **64,** 2210–2237.

Heymsfield, A. J., 1982: A comparative study of the rates of development of potential graupel and hail embryos in high plains storms. *J. Atmos. Sci.,* **39,** 2867–2897.

——, 2003: Properties of tropical and midlatitude ice cloud particle ensembles. Part II: Applications for mesoscale and climate models. *J. Atmos. Sci.,* **60,** 2592–2611.

——, and M. R. Hjelmfelt, 1984: Processes of hydrometeor development in Oklahoma convective clouds. *J. Atmos. Sci.,* **41,** 2811–2835.

——, and M. Kajikawa, 1987: An improved approach to calculating terminal velocities of plate-like crystals and graupel. *J. Atmos. Sci.,* **44,** 1088–1099.

——, A. Bansemer, and C. H. Twohy, 2007a: Refinements to ice particle mass dimensional and terminal velocity relationships for ice clouds. Part I: Temperature dependence. *J. Atmos. Sci.,* **64,** 1047–1067.

——, G.-J. van Zadelhoff, D. P. Donovan, F. Fabry, R. J. Hogan, and A. J. Illingworth, 2007b: Refinements to ice particle mass

dimensional and terminal velocity relationships for ice clouds. Part II: Evaluation and parameterizations of ensemble ice particle sedimentation velocities. *J. Atmos. Sci.,* **64,** 1068–1088.

Kessler, E., 1969: *On the Distribution and Continuity of Water Substance in Atmospheric Circulations. Meteor. Monogr.,* No. 32, Amer. Meteor. Soc., 84 pp.

Khairoutdinov, M., and Y. Kogan, 2000: A new cloud physics parameterization in a large-eddy simulation model of marine stratocumulus. *Mon. Wea. Rev.,* **128,** 229–243.

Khvorostyanov, V. I., and J. A. Curry, 2002: Terminal velocities of droplets and crystals: Power laws with continuous parameters over the size spectrum. *J. Atmos. Sci.,* **59,** 1872–1884.

Korolev, A. V., G. A. Isaac, and J. Hallett, 1999: Ice particle habits in Arctic clouds. *Geophys. Res. Lett.,* **26,** 1299–1302.

Leary, C. A., and R. A. Houze Jr., 1979: Melting and evaporation of hydrometeors in precipitation from the anvil clouds of deep tropical convection. *J. Atmos. Sci.,* **36,** 669–679.

Lin, Y.-L., R. D. Farley, and H. D. Orville, 1983: Bulk parameterization of the snow field in a cloud model. *J. Climate Appl. Meteor.,* **22,** 1065–1092.

Lord, S. J., H. E. Willoughby, and J. M. Piotrowicz, 1984: Role of a parameterized ice-phase microphysics in an axisymmetric, nonhydrostatic tropical cyclone model. *J. Atmos. Sci.,* **41,** 2836–2848.

Matson, R. J., and A. W. Huggins, 1980: The direct measurement of the sizes, shapes and kinematics of falling hailstones. *J. Atmos. Sci.,* **37,** 1107–1125.

McFarquhar, G. M., H. Zhang, G. Heymsfield, R. Hood, J. Dudhia, J. B. Halverson, and F. Marks Jr., 2006: Factors affecting the evolution of Hurricane Erin (2001) and the distributions of hydrometeors: Role of microphysical processes. *J. Atmos. Sci.,* **63,** 127–150.

Meyers, M. P., P. J. DeMott, and W. R. Cotton, 1992: New primary ice-nucleation parameterizations in an explicit cloud model. *J. Appl. Meteor.,* **31,** 708–721.

——, R. L. Walko, J. Y. Harrington, and W. R. Cotton, 1997: New RAMS cloud microphysics parameterization. Part II: The two-moment scheme. *Atmos. Res.,* **45,** 3–39.

Milbrandt, J. A., and M. K. Yau, 2005: A multimoment bulk microphysics parameterization. Part I: Analysis of the role of the spectral shape parameter. *J. Atmos. Sci.,* **62,** 3051–3064.

Mitchell, D. L., 1988: Evolution of snow-size spectra in cyclonic storms. Part I: Snow growth by vapor deposition and aggregation. *J. Atmos. Sci.,* **45,** 3431–3451.

——, 1994: A model predicting the evolution of ice particle size spectra and radiative properties of cirrus clouds. Part I: Microphysics. *J. Atmos. Sci.,* **51,** 797–816.

——, 1996: Use of mass- and area-dimensional power laws for determining precipitation particle terminal velocities. *J. Atmos. Sci.,* **53,** 1710–1723.

——, and A. J. Heymsfield, 2005: Refinements in the treatment of ice particle terminal velocities, highlighting aggregates. *J. Atmos. Sci.,* **62,** 1637–1644.

——, R. Zhang, and R. L. Pitter, 1990: Mass-dimensional relationships for ice particles and the influence of riming on snowfall rates. *J. Appl. Meteor.,* **29,** 153–163.

Morrison, H., and J. O. Pinto, 2006: Intercomparison of bulk cloud microphysics schemes in mesoscale simulations of springtime Arctic mixed-phase stratiform clouds. *Mon. Wea. Rev.,* **134,** 1880–1900.

——, and W. W. Grabowski, 2007: Comparison of bulk and bin warm-rain microphysics models using a kinematic framework. *J. Atmos. Sci.,* **64,** 2839–2861.

——, J. A. Curry, and V. I. Khvorostyanov, 2005: A new double-moment microphysics parameterization for application in cloud and climate models. Part I: Description. *J. Atmos. Sci.,* **62,** 1665–1677.

Ovtchinnikov, M., and Y. L. Kogan, 2000: An investigation of ice production mechanisms in small cumuliform clouds using a 3D model with explicit microphysics. Part I: Model description. *J. Atmos. Sci.,* **57,** 2989–3003.

Pruppacher, H. R., and J. D. Klett, 1997: *Microphysics of Clouds and Precipitation.* 2nd ed. Kluwer Academic, 954 pp.

Rasmussen, R. M., I. Geresdi, G. Thompson, K. Manning, and E. Karplus, 2002: Freezing drizzle formation in stably stratified cloud layers: The role of radiative cooling of cloud droplets, cloud condensation nuclei, and ice initiation. *J. Atmos. Sci.,* **59,** 837–860.

Reisner, J., R. M. Rasmussen, and R. T. Bruintjes, 1998: Explicit forecasting of supercooled liquid water in winter storms using the MM5 mesoscale model. *Quart. J. Roy. Meteor. Soc.,* **124,** 1071–1107.

Rogers, D. C., 1974: The aggregation of natural ice crystals. Rep. AR110, 91 pp. [Available from Department of Atmospheric Resources, College of Engineering, University of Wyoming, Laramie, WY 82072.]

Rutledge, S. A., and P. V. Hobbs, 1984: The mesoscale and microscale structure and organization of clouds and precipitation in midlatitude cyclones. XII: A diagnostic modeling study of precipitation development in narrow cold-frontal rainbands. *J. Atmos. Sci.,* **41,** 2949–2972.

Saleeby, S. M., and W. R. Cotton, 2004: A large-droplet mode and prognostic number concentration of cloud droplets in the Colorado State University Regional Atmospheric Modeling System (RAMS). Part I: Module descriptions and supercell test simulations. *J. Appl. Meteor.,* **43,** 182–195.

Seifert, A., and K. D. Beheng, 2001: A double-moment parameterization for simulating autoconversion, accretion and self-collection. *Atmos. Res.,* **59–60,** 265–281.

Smolarkiewicz, P. K., 1984: A fully multidimensional positive definite advection transport algorithm with small implicit diffusion. *J. Comput. Phys.,* **54,** 325–362.

——, and L. G. Margolin, 1998: MPDATA: A finite-difference solver for geophysical flows. *J. Comput. Phys.,* **140,** 459–480.

Szumowski, M. J., W. W. Grabowski, and H. T. Ochs III, 1998: Simple two-dimensional kinematic framework designed to test warm rain microphysical models. *Atmos. Res.,* **45,** 299–326.

Thompson, G., R. M. Rasmussen, and K. Manning, 2004: Explicit forecasts of winter precipitation using an improved bulk microphysics scheme. Part I: Description and sensitivity analysis. *Mon. Wea. Rev.,* **132,** 519–542.

Wang, P. K., and W. Ji, 2000: Collision efficiencies of ice crystals at low–intermediate Reynolds numbers colliding with supercooled cloud droplets: A numerical study. *J. Atmos. Sci.,* **57,** 1001–1009.

Wu, X., 2002: Effects of ice microphysics on tropical radiative–convective–oceanic quasi-equilibrium states. *J. Atmos. Sci.,* **59,** 1885–1897.

Young, K. C., 1974: The role of contact nucleation in ice phase initiation in clouds. *J. Atmos. Sci.,* **31,** 768–776.

Zhang, D.-L., and K. Gao, 1989: Numerical simulation of an intense squall line during 10–11 June 1985 PRE-STORM. Part II: Rear inflow, surface pressure perturbations and stratiform precipitation. *Mon. Wea. Rev.,* **117,** 2067–2094.